International Journal of Multiphase Flow 164 (2023) 104450

Contents lists available at ScienceDirect

International Journal of Multiphase Flow

journal homepage: www.elsevier.com/locate/ijmulflow

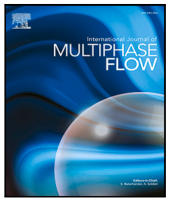

Insights on bubble encapsulation after drop impact on thin liquid films

Daniela F.S. Ribeiro [a,*], Miguel R.O. Panão [b], Jorge M.M. Barata [a], André R.R. Silva [a]

[a] AEROG – LAETA, University of Beira Interior, Covilhã, Portugal
[b] ADAI-LAETA, Mechanical Engineering Department, University of Coimbra, Rua Luis Reis Santos, 3030-788 Coimbra, Portugal

ARTICLE INFO

Keywords:
Droplet impingement
Bubble encapsulation
Floating bubble
Liquid film

ABSTRACT

The accurate understanding of the phenomenology of drop impact onto dry/ wetted and cold/heated surfaces is increasingly relevant to implement biofuels in civil aviation. The outcome of drop impact depends on the pre-impact conditions and a seldom researched event is the encapsulation of a bubble when this impact occurs on thin liquid films. Therefore, the goal of the experimental work reported is to investigate the mechanism of this bubble encapsulation. Results show that the mechanism leading to a bubble formation has two stages. In the first stage, after the drop impacts a steady liquid film, a prompt splash occurs followed by a crown splash. The uprising sheet propagates in an almost normal direction relative to the liquid film, but its radius at the base continues to expand, eventually leading to the inward collapse of the crown-bounding rim encapsulating air inside the dome. In the second stage, three different phenomenologies of bubble encapsulation can occur. At the top of the closed crown, one jet (phenomenology 1) or two jets are formed (phenomenologies 2 and 3). For phenomenology 2, the upward jet eventually collapses due to gravitational influence, while the downward jet continues to grow until it reaches the liquid film, attaching to it, stretching and detaching from the top at the hemispheric thin sheet, forming a bubble. In phenomenology 3, the upward jet is high enough to allow its breakup and ejection of one large droplet before the collapse of the upward jet. Many secondary droplets fall on the bubble and one of them will eventually break the dome, leading to more secondary atomization. Additionally, the first perturbation imposed on the liquid film by the droplet impact is studied and an empirical correlation is proposed for its propagation velocity. Finally, bubble geometry is investigated.

1. Introduction

A single droplet impinging upon a liquid film is a fundamental event in multiple applications such as fuel injection in internal combustion engines, corrosion of turbine blades, meteorite impact upon space vehicles, surface cooling, spray painting, coatings, and also in natural phenomena like soil erosion by raindrops. In previous works, Ribeiro et al. (2018) investigated the outcome of these impacts with the goal of assessing the implications of implementing biofuels in internal combustion engines. Six different phenomena were observed and one of them involved bubble entrapment, which despite being reported in the literature, the underlying physics is still a question open for further research. Therefore, the purpose of the work presented here is to improve the knowledge of thermofluid dynamic mechanism generating bubble encapsulation or floating bubble, on the impact of a single droplet onto thin and shallow liquid films, corresponding to the trapping of air after the closing of an uprising crown sheet.

The identification of the bubble encapsulation event occurred sporadically over the years. In 1908, Worthington (1908) dedicated a section of his book to the formation of bubbles for the impact of droplets of size D_0 from high impact distances onto deep pools. When increasing the impact height to evaluate its influence on the crater depth, a new phenomenon appeared, described by the closure of the crater "mouth" and the formation of a bubble. The physical explanation included that both the upward liquid flow feeding the crown rim and the consolidating effect of surface tension promoted the formation of the bubble structure. Also, if the impact velocity is not sufficiently high, the crown almost closes or closes for an instant before quickly reopening, indicating the existence of a threshold in the pre-impact operating conditions for the onset of this event.

A few decades later, Engel (1966) observed this phenomenon while studying the impact of single droplets upon liquid targets to simulate micrometeorites shocking on spatial vehicles, focusing on the cavities originated from these impacts. If the impact energy exceeded a certain threshold, Engel (1966) observed the upper edge of the crown-thin cylindrical sheet rising at the top of the cylindrical wave will, at least, neck in and close forming a spherical bubble above the cavity. At the

* Corresponding author.
E-mail addresses: daniela.santo.ribeiro@ubi.pt (D.F.S. Ribeiro), miguel.panao@dem.uc.pt (M.R.O. Panão), jbarata@ubi.pt (J.M.M. Barata), andre@ubi.pt (A.R.R. Silva).

https://doi.org/10.1016/j.ijmultiphaseflow.2023.104450
Received 2 November 2022; Received in revised form 8 March 2023; Accepted 20 March 2023
Available online 30 March 2023

Nomenclature

a, b	Terms of equation D_p^*
D_0	Initial droplet diameter (mm)
D_B	Bubble diameter (mm)
D_B^*	Dimensionless bubble diameter $D_B^* = D_B/D_0$
D_c	Crown diameter (mm)
D_c^*	Dimensionless crown diameter $D_c^* = D_c/D_0$
D_p	Propagation diameter (mm)
D_p^*	Dimensionless propagation diameter $D_p^* = D_p/D_0$
h_B	Bubble height (mm)
h_B^*	Dimensionless bubble height $h_B^* = h_B/D_0$
h_f	Film thickness (mm)
Oh_D	Ohnesorge number $Oh_D = \sqrt{We_D}/Re_D$
Re_D	Reynolds number $Re_D = \rho D_0 U_0/\mu$
t	Time after impact (s)
t_{bubble}	Bubble formation time (s)
U_0	Droplet impact velocity (m/s)
U_p	Propagation velocity (m/s)
U_p^*	Dimensionless propagation velocity $U_p^* = U_p/U_0$
We_D	Weber number $We_D = \rho U_0^2 D_0/\sigma$

Other Symbols

α_c	Crown angle (°)
δ_f	Dimensionless film thickness $\delta_f = h_f/D_0$
μ	Viscosity (Pa·s)
ρ	Density (kg/m^3)
σ	Surface Tension (N/m)
τ	Dimensionless time $\tau = tU_0/D_0$
τ_{bubble}	Dimensionless bubble formation time $\tau_{bubble} = t_{bubble}U_0/D_0$

closure point, a liquid jet develops and moves downward via the cavity floor, while an upward-moving jet generated by receding forces on the cavity, contacts, and mixes with the downward-moving jet.

Later, Pan et al. (2008) focused their work on the impact of high-speed droplets upon liquid layers of thickness h_f and reported that, at large droplet Weber numbers ($We_D \geq 2570$) and thick liquid films ($\delta_f = h_f/D_0 > 1$), the ejected crown closes and forms a bubble. The Weber number describes the ratio between the inertial and surface tension forces, $We_D = \rho D_0 U_0^2/\sigma$, with ρ and σ being the density and surface tension of the liquid, respectively, and U_0 [m/s] and D_0 [mm] are the drop impact velocity and diameter, respectively. They also obtained this outcome for thinner liquid films while increasing the impact energy up to $We_D = 4000$. Additionally, Pan et al. (2008) observed the transition boundary for the onset of bubble entrapment decreased monotonically with the increase of the dimensionless film thickness and stabilized when the film thickness became larger than the cavity depth.

After encapsulating a bubble, the impact of tiny droplets onto its dome can disrupt its thin sheet, and form an additional sample of micro-droplets. The ability to predict the outcome is relevant, for example, for the emission of airborne particles with respect to the safety of nuclear facilities is related to drop impact events (Motzkus et al., 2009). Other hydrodynamic mechanisms besides bubble bursting would be prompt splash and finger pinching. Motzkus et al. (2009) reported that for low surface tension fluids, bubble bursting provides a high production of droplets with sizes smaller than 15 μm. In their experiments, the bubble sheet thickness progressively becomes thinner under the effect of the rising bubble and the liquid drainage towards the film. When the hemispherical thin sheet reaches a critical thickness, it breaks and produces tiny droplets. Several parameters influence the number and size of the emitted droplets: bubble size, air–liquid surface tension, liquid viscosity, and thickness of the bubble sheet. However, they only observed one case with the formation and break up of bubbles (Motzkus et al., 2009), which is not enough to develop any criterion, and the physics of bubble formation remains absent from that work.

Later, Pan and Hung (2010) extended the knowledge about the bubble entrapment event, mentioning that the enclosure of the crown resulted from the bending of the upwardly ejected sheet by gravitational forces. The main goal of their study was to create transition boundaries for the different outcomes of a droplet impinging upon a thin liquid layer. These authors solely observed closed crowns at very high impact velocities ($U_0 = 11.15$ m/s), and the bubble trapped inside could cause some underwater perturbations, eventually, affecting the transport of fluid or transmission of sound waves. The gravitational effect also led to the emergence of two jets, upwards and downwards, but, again, little is added to the physics of the hydrodynamics mechanism underlying the formation of these encapsulated bubbles.

While pursuing a simulation of diesel droplets impinging upon the lubricating oil film covering the combustion chamber walls, Geppert et al. (2016) detected two additional phenomena – jet and bubble formation – and their occurrence was not occasional. Both the central jet and the encapsulated bubble had been already detected for one-component interactions (droplet and liquid film of the same fluid), but mainly for thicker liquid films ($\delta_f \geq 0.5$). Thus, it is reasonable to assume that the dynamic of splashing is far more complex than the typical deposition/splashing boundary. In their experiments, the bubble formation occurred for $\delta_f \geq 0.2$ and $We_D > 1100$, and they agreed with Worthington (1908) about the effects which originate the bubble. Namely, an upward flow feeding liquid to the crown rim and the action of surface tension. Both effects extend the lifetime of splashing eventually leading to the closing of the crown and the formation of a stable bubble. However, the bubble bursting is solely attributed to the thinning of its wall film until it reaches a critical breakup point.

In their review work, Liang and Mudawar (2016) recognize that a few authors (Motzkus et al., 2009; Ninomiya and Iwamoto, 2012; Guo et al., 2010) reported the existence of narrow or closed rims underlying bubble encapsulation, emphasizing its dependence on the dimensionless film thickness and the impact velocity.

To help understand the main differences and similarities between the impact conditions where bubble encapsulation was observed in a previous work (Ribeiro et al., 2018) and in other studies mentioned in the literature, Fig. 1 synthesizes the most relevant information about bubble encapsulation visualization over the years, including the primary goal of each work. Despite observing this phenomenon, none of the authors focused on the characteristic morphology of bubble encapsulation or detailedly investigated the impact conditions originating the bubble formation.

In a previous study, Ribeiro et al. (2020a) reported detailed experimental observations of the bubble encapsulation phenomenon for $We_D = 1650$ and $\delta_f = 0.5$. The impact velocities exceed the 10 m/s in some of the studies mentioned, and the cases where the impact conditions were more similar to the one described by Ribeiro et al. (2020a) belong to Geppert et al. (2016) and Motzkus et al. (2009).

Despite being mentioned, bubble encapsulation was never deeply investigated, nor were its morphological characteristics in detail. Therefore, this work reports a preliminary study made to fill the lack of knowledge about bubble encapsulation in the literature. Understanding bubble encapsulation formation mechanisms and main features is important to assess if this phenomenon should be encouraged or avoided. Encouraged if a longer phenomenological lifetime and enhanced production of secondary atomization are useful, or avoided if the tiny secondary droplets originated by the bubble bursting increase the

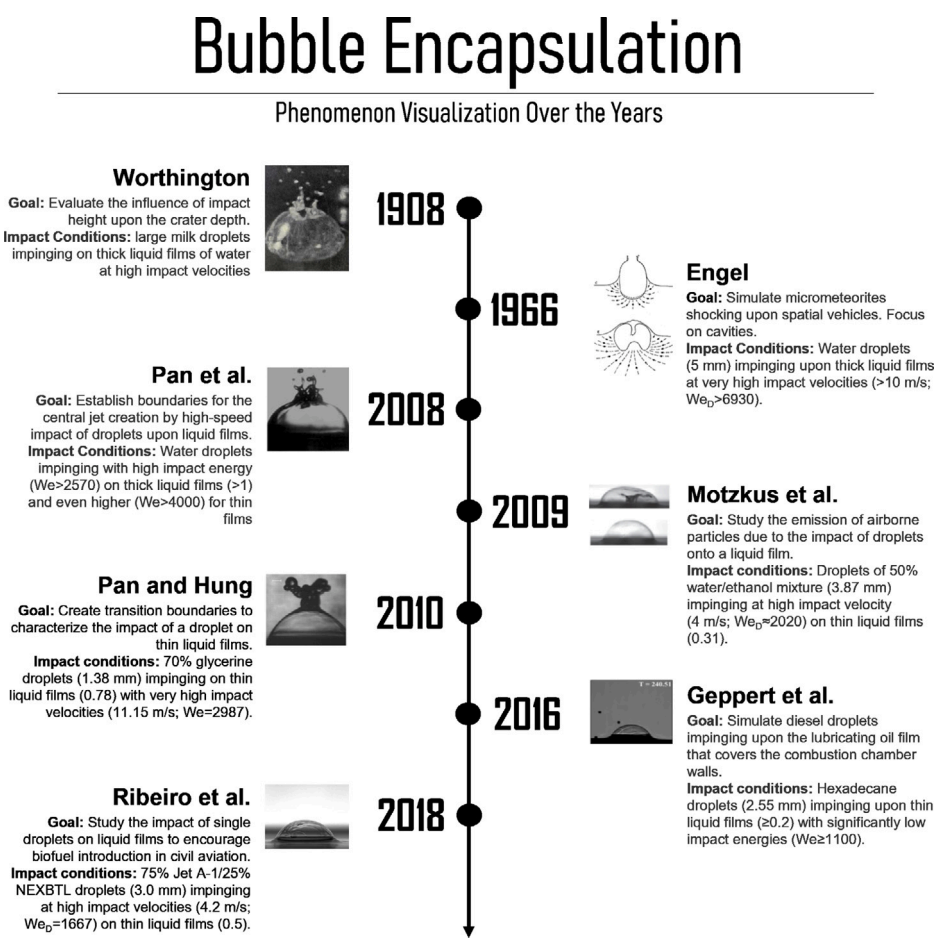

Fig. 1. Bubble encapsulation visualization over the years.

airborne particles ejection, for example, affecting pollutant emissions. Following previous research on bubble encapsulation, the fluid used is a mixture of 75% Jet A-1 and 25% NExBTL. Jet A-1 is a conventional Jet Fuel (JF), and NExBTL (Neste Renewable Diesel) is a biofuel of type of HVO (Hydro-processed Vegetable Oil). The main research question of this study is establishing the general characteristics of this bubble encapsulation event. The principal objective is to classify the different phenomenological categories of bubble encapsulation generally, and considering their interest in the future simulation of the event, the specific objectives focus on: (i) the dynamic characteristics of the initial stages, namely, the first propagation wave after impact because a significant part of the encapsulated bubble size forms in a short time interval compared to the total time for bubble formation; (ii) and the bubble's geometric features when fully formed. Particular attention is given to the influence of dimensionless film thickness upon the onset of bubble encapsulation at room temperature and pressure. The visualization of the bubble encapsulation generated by drop impact on thin films ($\mathcal{O}(\delta_f) \sim 10^{-1}$) aims to understand the onset of its occurrence, phenomenologies, main features, and physical significance. The next section describes the experimental setup used to study the phenomenon through high-speed imaging and sets the operating conditions explored in the results and discussion section.

2. Experimental method and setup

The experimental setup has one configuration to acquire images of the bubble encapsulation from the side, and another to visualize from below. Therefore, the lateral and bottom perspectives are acquired successively and not simultaneously since only one high-speed camera is available. The configuration visualizing from the side enables the measurement of bubble height and diameter, while the visualization from below allows measuring bubble diameter and the propagation velocity of the first perturbation imposed on the liquid film. The experimental facility shown in Fig. 2 consists of four main sections: image acquisition system (1, 2, 6), drop dispensing system (3, 4), impact surface (5), and impact site illumination (7, 8, 9).

A high-speed digital camera Photron FASTCAM mini UX50 with 1.3 Megapixel resolution acquires images at frame rates up to 2000 fps (frames per second) and up to 160,000 fps at reduced image resolution. A Macro Lens Tokina AT-X M100 AF PRO D with a minimum focal length of 0.3 m was also used. For all the acquired images, the resolution was 1280×1024, the exposure time was set to 1/5120 s, and the frame rate fixed at 2000 fps. The droplet dispensing system consists of a syringe pump NE-1000 connected to a straight-tip stainless steel needle. The syringe pump supplies a volumetric flow rate of 0.5 ml/min allowing the droplet to leave the needle when gravity exceeds the surface tension forces. The impact surface is a perspex container designed to ensure the walls of the container do not interfere with the outcome while holding the liquid film. The illumination of the impact site is vital to improve the quality of the images acquired. Therefore, the room is kept dark to restrict illumination to the backlight source set of LEDs parallel to the droplet falling plan for the side images, and another set of LEDs parallel to the impact surface for the bottom images. In addition, for the side images, a diffusion glass placed between the light source and the camera ensures a uniform background in the experiments.

The experiments were performed at room temperature and atmospheric pressure, and as previously stated, the fluid used blends 75% Jet A-1 and 25% NExBTL, due to previous studies (Ribeiro et al., 2018, 2020a,b; Ferrão et al., 2020), and its physical properties were

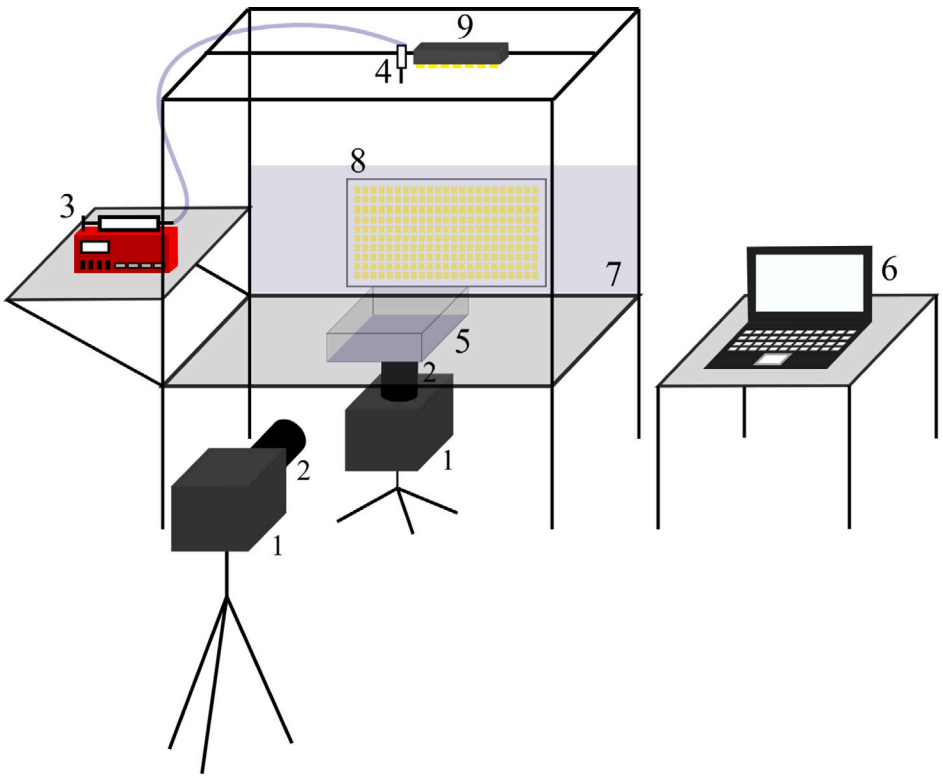

Fig. 2. Scheme of the experimental facility: (1) high-speed camera; (2) macro lens; (3) syringe pump; (4) stainless steel needle; (5) liquid film container; (6) computer; (7) diffusion glass; (8 and 9) set of LEDs.

measured: density, $\rho = 795$ kg/m^3, surface tension, $\sigma = 25.5$ mN/m, and viscosity, $\mu = 1.44 \times 10^{-3}$ Pa s. The needle used has an inner diameter of 1.5 mm, generating 3.0 mm droplets, and the impact velocity is kept constant at $U_0 = 4.2$ m/s, providing a set of constant dimensionless numbers, including the Weber (We_D), the Reynolds (Re_D), and the Ohnesorge (Oh_D) numbers. The Weber number relates the droplet kinetic energy and surface energy, $We_D = \frac{\rho U_0^2 D_0}{\sigma} = 1650$. The Reynolds number is defined by the ratio between the inertial and viscous forces, $Re_D = \frac{\rho U_0 D_0}{\mu} = 6956$. Finally, by relating the last two dimensionless numbers, the Ohnesorge number can be obtained as $Oh_D = \frac{\mu}{\sqrt{\rho \sigma D_0}} = \frac{\sqrt{We}}{Re} = 5.84 \times 10^{-3}$.

The liquid film thickness is produced by volume. The container has dimensions of 20×20 cm^2 and right-angled edges. Thus, the volume of fluid necessary to have a specific thickness was calculated and this volume was inserted inside the container. Finally, the thickness is confirmed by using the high-speed digital camera. Producing such thin liquid films is difficult if the contact angle between the fluid and the surface is considerably high. However, in this case, the mixture with Jet A-1 and NExBTL shows a superhygrophilic behavior with the Perspex. The term "hygro" is used for liquids in general, while the term "hydro" is only valid for water. This superhygrophilic behavior allows the production of very thin liquid films. For each set of experimental conditions, 10 experiments were made. Thus, it was necessary to guarantee that these droplets will not affect the thickness of the liquid film. A study was developed and it was concluded that these 10 droplets will not change the thickness of the liquid film in more than 1%. Therefore, it was assumed that all 10 experiments were made using the same liquid film. The liquid film is exchanged after a set of experiments with the same experimental conditions. In this study, the dimensionless liquid film ranged between $0.1 < \delta_f < 1.0$. This is the only impact parameter not kept constant since the main goal of this study is to understand its role in the onset of bubble encapsulation.

Image data processing is essential to allow the measurement of the phenomenon's main features. In this case, these measurements include the bubble height and diameter, and the propagation velocity. Thus, the algorithm for image treatment developed using the software MATLAB begins by subtracting the background from the original image. Then, through binarization, the image is transformed into a matrix of zeros and ones, allowing us to measure the different parameters by counting the number of pixels or identifying the position of a certain boundary. Finally, one calculates the sizes of droplets by multiplying the values obtained by the calibrated resolution of the image (34.6 μm/pixel ± 5.47%). The height and diameter values have an accuracy of ±0.03 mm and the uncertainty in the impact velocity is ±0.006 m/s.

A Perspex container was used to hold the liquid film due to its transparency and also its wettability since it shows a superhygrophilic behavior with the mixture of jet fuel and biofuel used, which allows the production of very thin liquid films. The optical distortion may affect the measuring precision of the images through the transparent wall. Therefore, to calculate the pixel size, a reference was placed exactly at the droplet impact point and captured by the high-speed camera. In this way, the optical distortion is already accounted in the determination of the pixel size.

3. Results and discussion

This section begins with explaining the bubble formation event using the results obtained from high-speed visualization. The images show two perspectives. The most common is the side view, while the novelty resides in the observations made below.

After explaining the phenomenon under study, the analysis focus on two features related to the bubble formed after the droplet impact on the liquid film, the thickness of the hemispherical liquid sheet and the cavity underneath the bubble. Finally, some considerations begin with the effect of different dimensionless film thicknesses on the propagation of the first film perturbation and the bubble geometry.

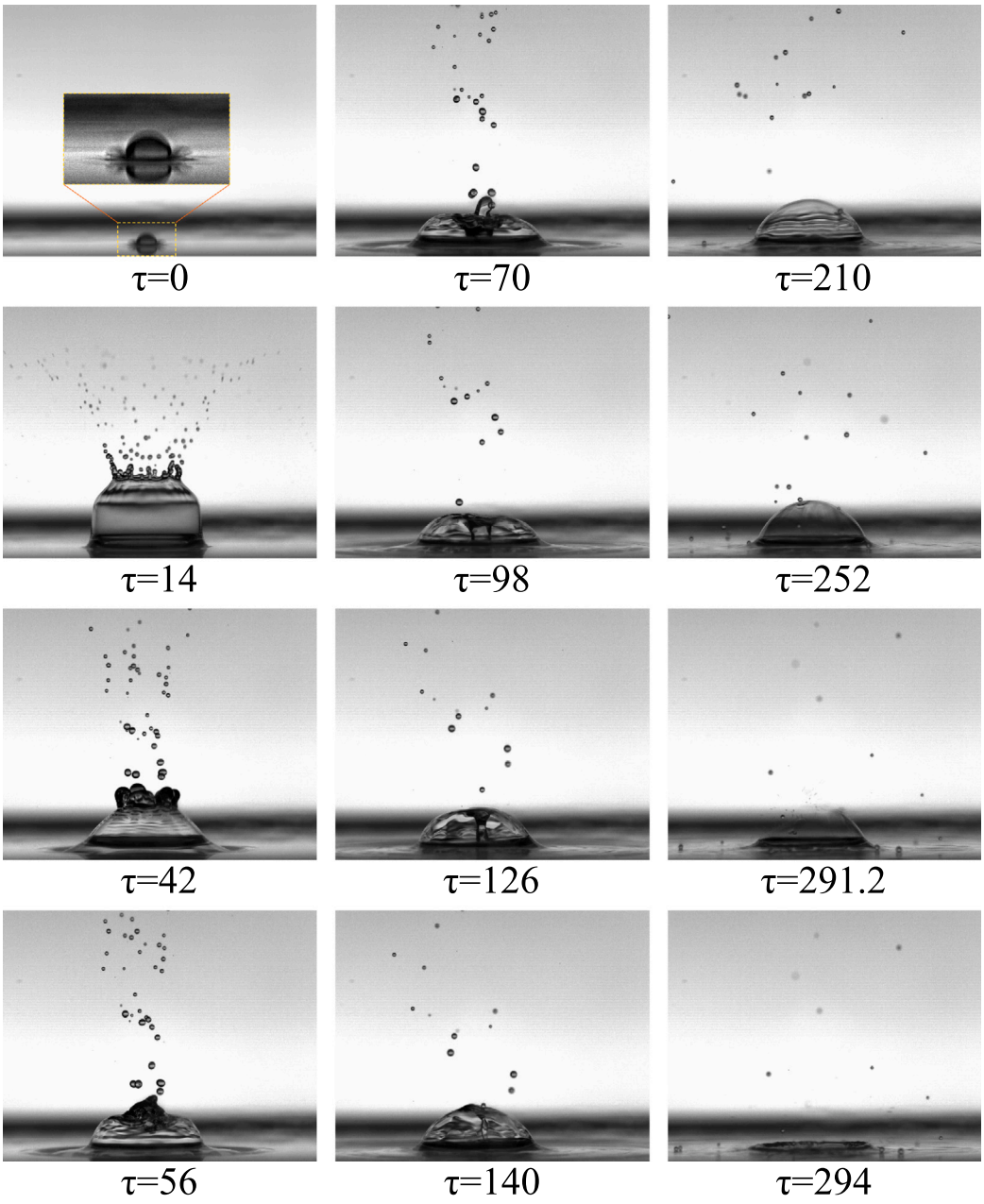

Fig. 3. A sequence of images showing bubble encapsulation for the following impact conditions: 75% JF/25% HVO, D_0 = 3.0 mm, U_0 = 4.2 m/s, and δ_f = 0.5.

3.1. Phenomenologies of bubble encapsulation

Similarly to other authors, for the dimensionless film thickness of $\delta_f = 0.5$, the impact velocity for which bubble encapsulation occurred with 100% repeatability was $U_0 = 4.2$ m/s. The image sequence shown in Fig. 3 allows the lateral visualization of the main hydrodynamic structures in bubble encapsulation for different dimensionless time instants after impact with $\tau = tU_0/D_0$, where t is time after the moment the droplet touched the liquid film considered as $t = 0$ s. To acquire these images the camera has an angle of ≈10° with the horizontal plane. The camera was only inclined for the visualization imaging. In the remaining experiments the camera was parallel to the horizontal liquid film. Fig. 4 shows the phenomenon from a bottom perspective.

After impact on a steady liquid film, the droplet prompt splashes ($\tau = 0$), followed by the formation of an uprising crown producing secondary droplets from instabilities in its bounding rim ($\tau = 14$). In the first stages, the uprising sheet propagates almost normally to the liquid film, but the radius of the crown base continues to expand, eventually leading to the inward gradual closing of the crown-bounding upper rim. Several secondary droplets are ejected by the fingering breakup at the top of the crown, with a size proportional to the transient accumulation of mass in the rim as the splashing mechanism unfolds. This inward collapse occurs at $\tau = 42$. The closing of the crown at the top entraps air and begins forming a bubble-like shape ($\tau = 56$), and two jets ($\tau = 70$). One jet moves upwards and the other in a downward direction. While the upward jet eventually stops and recedes due to gravitational forces, the downward jet reaches the horizontal liquid film ($\tau = 98$), attaches to it, stretches, and detaches from the top at the hemispheric thin-sheet ($\tau = 126$ and $\tau = 140$). After this detachment, at $\tau = 210$, a bubble fully formed remains on the liquid film.

Meanwhile, many secondary droplets strike the bubble dome ($\tau = 252$) and one of them will eventually break it and generate even more secondary droplets ($\tau = 291.2$). These secondary droplets will impinge immediately on the liquid film inducing more perturbations ($\tau = 294$).

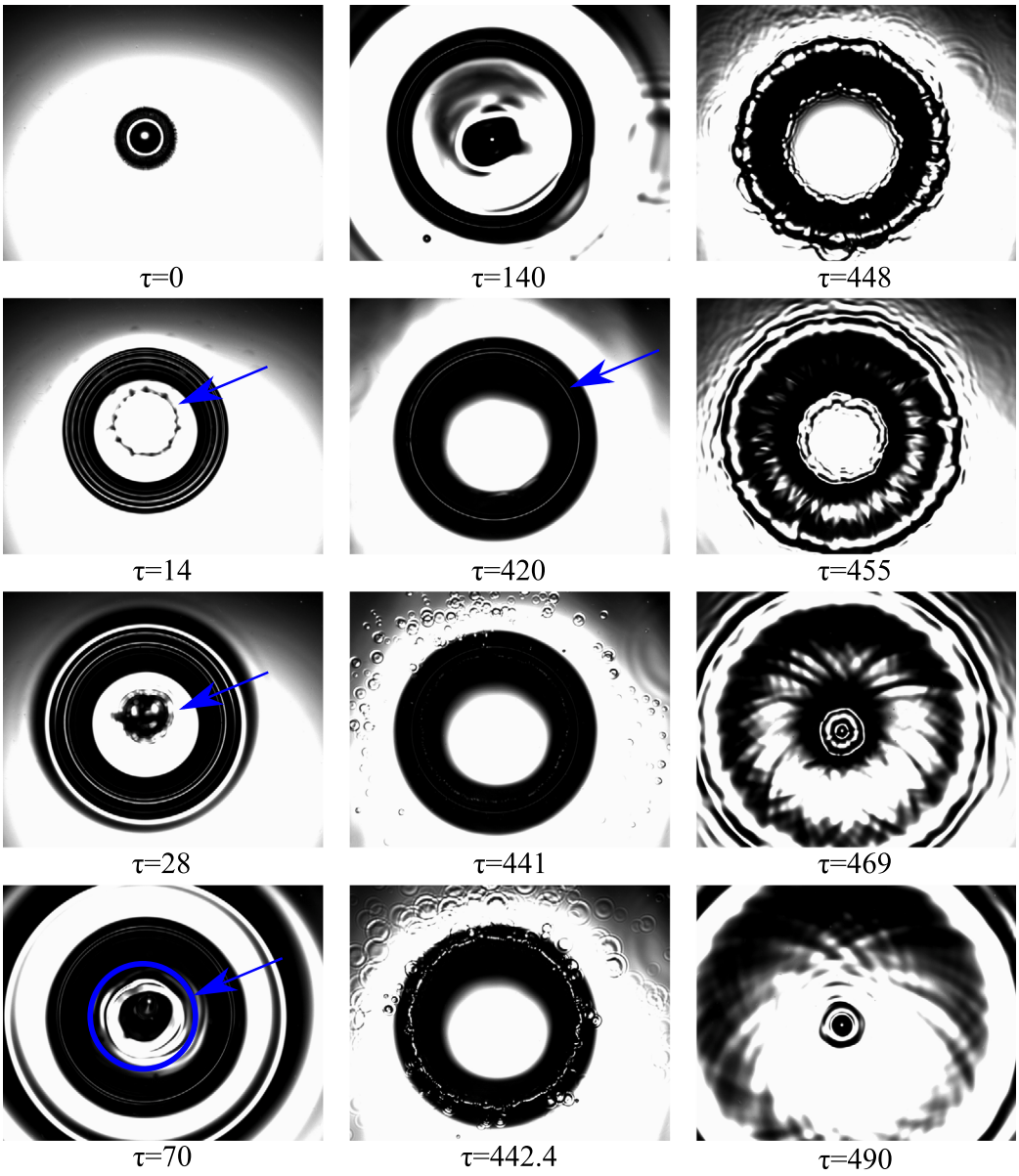

Fig. 4. Sequence of images showing bubble encapsulation from below for the following impact conditions: 75%JF/25% HVO, $D_0 = 3.0$ mm, $U_0 = 4.2$ m/s, and $\delta_f = 0.5$.

In time, the perturbations cease and the liquid film returns to the initial steady condition.

As stated by Motzkus et al. (2009), the liquid in the bubble's hemispherical thin-sheet progressively becomes thinner and more susceptible to break due to the impact of secondary droplets previously created by the crown splash. The wavy pattern observed at $\tau = 210$ in Fig. 3 evidence the draining of liquid from the bubble thin-wall to the liquid film.

A phenomenological feature worth mentioning is the constant height of the crown liquid sheet that propagated first in the direction normal to the liquid film ($\tau \leq 4.2$). Afterward, during a radial expansion for $4.2 < \tau < 25.9$, this height remains unaltered, as shown in Fig. 5, but also the crown angle at 90°. Relatively to the constant crown angle, Wang and Chen (2000) also observed a perpendicular uprising of the crown wall relative to the horizontal liquid film for the dimensionless film thickness of 0.5, considering a higher Weber number ($We_D = 2010$), but a six times significantly lower Reynolds number ($Re_D = 1168$), implying a role played by viscous forces allowing a radial expansion of the crown base. Additionally, Fedorchenko and Wang (2004) reported that the crown angle depends entirely on the liquid film thickness, regardless of the impact velocity and liquid physical properties. Nonetheless, they stated that for $\delta_f \geqslant 0.25$ the angle is constant and equal to 90°. Furthermore, recently Lamanna et al. (2022) showed that the viscous losses are negligible during the spreading phase but only in the early stage of crown propagation. However, while decreasing the liquid film thickness they become increasingly significant.

The morphological structures associated with the crown dynamics leading to bubble encapsulation seem related to the expansion of the annular crown base and the mass transfer in the crown liquid sheet. Therefore, the hypothesis is to observe the phenomenon from below to investigate its dynamics using the perspective of the floating bubble. In this sense, the high-speed digital camera, mounted below the glass supporting the Perspex container, captured a sequence of images depicted in Fig. 4. It is important to remember that only one high-speed digital camera was available and the images in Figs. 3 and 4 do not correspond to the same droplet impact, but two separate droplet impacts with the same impact conditions.

The droplet impinges upon the steady liquid film ($\tau = 0$), and shortly after, the crown sheet rises and starts bending inwards ($\tau = 14$),

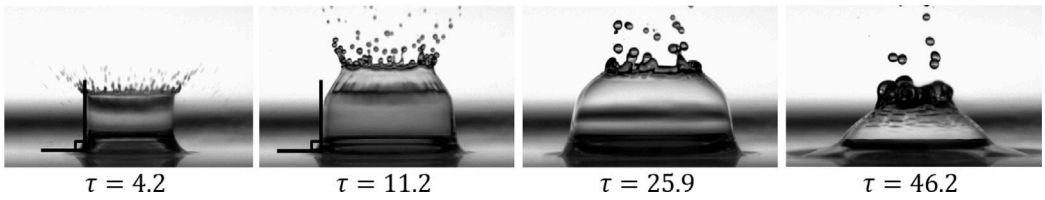

Fig. 5. Evolution of the crown sheet angle during the formation of bubble encapsulation.

as visualized by the bounding rim of the crown sheet pointed in this frame by an arrow. The crown sheet closes at $\tau = 28$ by the increase of mass of the crown rim fed by the liquid sheet, plus surface tension forces, indicated by the arrow in this frame. At $\tau = 70$, in the center (delimited by a circle), the dark area corresponds to the downward jet connecting to the bottom of the crater (see frames $\tau = 70$ and 98 of Fig. 3 showing this morphology from the side). Nothing could be concluded about the upward jet since it cannot be seen from this visualization perspective. The downward jet continues its motion to the cavity floor ($\tau = 140$). In this frame, it is easily perceived the bubble-thin liquid sheet by the large white circle, and the jet by the darker circle in the middle. Later, at $\tau = 420$, the downward jet detaches from the thin-liquid dome, forming an empty bubble, the thin white circumference within the dark circle, pointed by the arrow. To help visualization see frame $\tau = 210$ in Fig. 3. At this time, the liquid film is almost steady, and the dark portion of the circle identifies the curvature of the bubble dome attached to the liquid film. In this case, at $\tau = 441$ the bubble breaks by reaching the critical thickness of the hemispherical liquid sheet or by the impingement of a tiny secondary droplet (frame $\tau = 252$ in Fig. 3). It is impossible to ensure that from this point of view. The following frames show the perturbations imposed on the liquid film by the bubble bursting. The evolution of the pattern created at the liquid film by the breakup of the bubble is shown in frames $\tau = 448$ to $\tau = 490$.

By virtue of these images from below, it is possible to accurately measure the bubble diameter and also the propagation velocity of the first perturbation imposed on the liquid film by the droplet impact addressed ahead. Comparing both sequences of images is easy to infer that the phenomena or timescales are different. However, the bubble's lifetime strongly depends on the number of secondary droplets that can puncture the bubble's dome when it is thin enough.

During the experiments, different impact conditions lead to different phenomenologies in the bubble formation. These differences are related to the jet formation and evolution from the crown closure point. In summary, there are three different paths to obtain the same outcome, bubble encapsulation. Fig. 6 shows the evolution of the phenomena morphology depending on the three different phenomenologies identified:

- Phenomenology 1 - formation of a downward jet after the crown closure, Fig. 6(a);
- Phenomenology 2 - formation of a downward and an upward jet on the crown closure point, Fig. 6(b);
- Phenomenology 3 - formation of a downward and an upward jet on the crown closure point, combined with the ejection of large droplets due to the upward jet breakup, Fig. 6(c).

To distinguish the different phenomenologies, a visualization analysis was conducted. The major difference between the three phenomenologies is related to the existence or not of an upward jet and its consequent breakup. Through a "naked" eye analysis, the three different phenomenologies were identified. However, some events are close to the transition between phenomenology 1 and 2. The protrusion resulting from the merging of the jets at the top of the crown can be confused with a small upper jet. In these cases, the height of this jet/protrusion was measured using the post-processing algorithm. If its height increases, it is considered phenomenology 2 since a small jet is formed and ascends. If the height does not increase then it is just a protrusion formed by the merging of the jets at the top of the crown and it is classified as phenomenology 1.

Table 1
Phenomenologies observed depending on the dimensionless film thickness δ_f and the correspondent dimensionless bubble time τ_{bubble}. The number of experiments (exp.) for each phenomenology is defined. The uncertainty values are absolute and obtained with a confidence interval of 95%.

δ_f	Phenomenology	τ_{bubble}
0.4	1 (3 exp.), 2 (3 exp.), 3 (4 exp.)	80.8 ± 9.4
0.5	1 (5 exp.), 2 (5 exp.)	134.2 ± 5.7
0.6	2 (10 exp.)	155.0 ± 9.7
0.7	2 (10 exp.)	107.8 ± 11.7
0.8	2 (10 exp.)	101.6 ± 11.4
0.9	2 (10 exp.)	90.7 ± 4.8
1.0	2 (10 exp.)	90.7 ± 3.9

Fig. 3 is an example of the phenomenology 2. The initial stages in the phenomenology 1, shown in Fig. 6(a) are similar to phenomenology 2. However, in this phenomenology at $\tau = 56$ only a downward jet forms, instead of two in opposite directions. Later, the liquid is drained by the jet ($\tau = 112$) until its detachment from the hemispherical sheet's top ($\tau = 133$), forming an empty bubble at $\tau = 175$.

On the other hand, phenomenology 3, Fig. 6(c), has exactly the same formation as phenomenology 2, but due to the excess of kinetic energy, the upward jet is larger ($\tau = 49$) and breaks into a large secondary droplet ($\tau = 77$). This droplet heavily falls on the hemispherical dome. In some cases, it merges with the liquid sheet or slips from the hemispherical walls towards the liquid film, or in a few cases, the large secondary droplet immediately breaks the bubble.

Table 1 shows the different phenomenologies observed depending on the dimensionless film thickness of the liquid film δ_f. For $0.6 \leq \delta_f \leq 1.0$ only phenomenology 2 was observed on the 10 experiments performed. On the other hand, for $\delta_f = 0.4$ all three different phenomenologies were observed and for $\delta_f = 0.5$ both phenomenologies 1 and 2 were observed. The dimensionless bubble time $\tau_{bubble} = t_{bubble} U_0 / D_0$, with t_{bubble} being the formation time of the bubble, was measured and included in Table 1. For the events were only phenomenology 2 was observed the dimensionless bubble time seems to decrease while increasing the dimensionless film thickness, which may be caused by the increased liquid volume of the crown.

A final morphological consideration is the influence of the dimensionless film thickness in the bubble formation. In this case, the experiments performed considered dimensionless film thicknesses between 0.1 and 1, with steps of 0.1. For thinner liquid films ($\delta_f < 0.2$), only prompt and crown splash were observed, and the phenomenon was too quick to allow crown closure. For $\delta_f = 0.2$ and $\delta_f = 0.3$, some impacts resulted in bubble encapsulation but in less than 50% of the cases. For $\delta_f = 0.4 - 1$, there was 100% occurrence of bubble formation and the crown sheet angle seems almost perpendicular to the horizontal liquid film for all the cases. Hence, the crown sheet angles obtained agree with Fedorchenko and Wang (2004) conclusions. On the other hand, a crown sheet angle normal to the horizontal liquid film is not restricted to $\delta_f = 0.5$ as Wang and Chen suggested (Wang and Chen, 2000). According to Pan et al. (2008), the factor for closing the crown depends on the balance between the upward motion of the sheet and

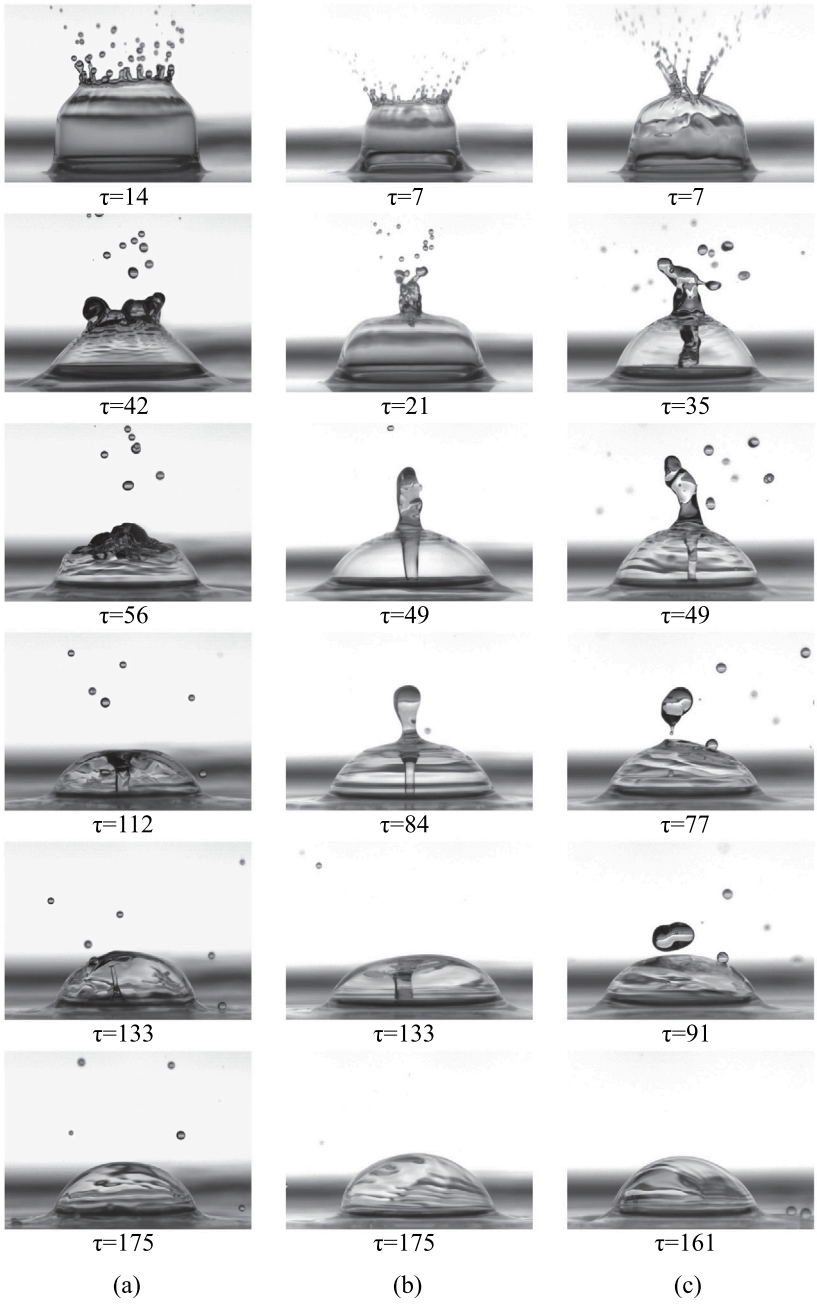

Fig. 6. Different phenomenologies during bubble formation for a 3.0 mm droplet of 75% jet fuel/25% HVO mixture at $U_0 = 4.2$ m/s and $We_D = 1650$: (a) Phenomenology 1 - only a downward jet is formed by the crown closure for $\delta_f = 0.5$; (b) Phenomenology 2 - both a downward and an upward jet are formed on the crown closure point for $\delta_f = 0.6$; (c) Phenomenology 3 - both a downward and an upward jet are formed on the crown closure point, combined with the ejection of large droplet due to the upward jet breakup for $\delta_f = 0.4$.

the downward pull of gravity. Therefore, one would expect to reduce the likelihood of enclosing the crown by lowering the dimensionless film thickness since the inertia of the uprising liquid sheet weakens. The experiments performed in this work validate this assessment since bubble encapsulation never occurred for $\delta_f = 0.1$ and only some events were observed for $\delta_f = 0.2$ and $\delta_f = 0.3$. Moreover, increasing the dimensionless film thickness apparently leads to thickening the hemispherical liquid sheet, as visualized in Fig. 7 and it extends the time until the bubble bursts (Geppert et al. (2016) also detected this).

Regarding a possible boundary for the bubble encapsulation occurrence, much more experiments are necessary including more fluids, impact velocities, and initial droplet diameters. Nevertheless, for this fluid, bubble encapsulation forms at a minimum Weber number of $We_D = 1650$ for $\delta_f \geq 0.2$, and for 100% occurrence: $\delta_f \geq 0.4$. Pan et al. (2008) observed it for $We_D \geq 2570$ and $\delta_f > 1$, and for $We_D \geq 4000$ for thinner liquid films. Additionally, Geppert et al. (2016) saw this phenomenon for $We_D > 1100$ and $\delta_f \geq 0.2$. Considering all the studies reviewed, none of them considered other dimensionless numbers. Therefore, the only comparative element is the minimum Weber number for the bubble encapsulation occurrence combined with the dimensionless film thickness used, justifying the search for a boundary that predicts bubble formation. However, the Weber number excludes the effect of viscous forces that may play a relevant role in the radial expansion of the crown base.

The cavity formed underneath the bubble and the physical parameters which govern bubble encapsulation are worthy of attention. If the

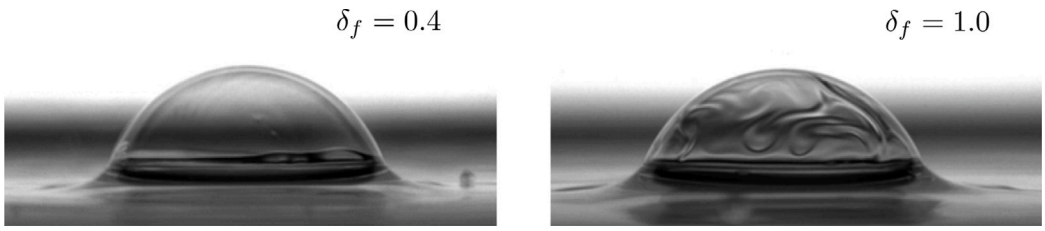

Fig. 7. Bubble hemispherical sheet becomes thicker by increasing the dimensionless film thickness.

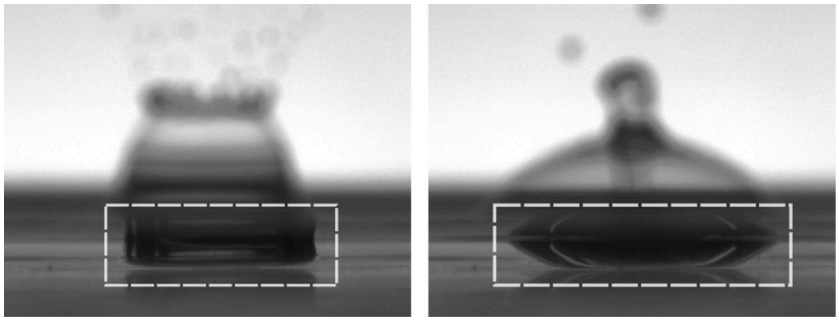

Fig. 8. Cavity formed after drop impact evidencing its collision with the solid surface for $We_D = 1650$ and $\delta_f = 0.5$.

liquid film is thin ($\delta_f < 1$), the impact crater collides with the solid surface at the bottom, as shown in Fig. 8.

After the droplet impingement on the liquid film, the cavity immediately touches the bottom of the container, eventually inducing capillary instabilities on the morphological structures leading to bubble encapsulation. Roisman et al. (2008) mentioned that capillary waves arrive on the surface of the cavity and a similar event seems present.

3.2. Propagation of the first film perturbation

A single droplet impinging upon a steady liquid film creates a wave perturbation spreading radially along the liquid film. In this study, the first perturbation visualized on the liquid film corresponds to the first wave propagating on its free surface. A detailed analysis is worthy because the propagation of the first film perturbation corresponds to a significant part of the encapsulated bubble size formed in a short time interval compared to the total amount it takes to form the bubble. Also, the ability to predict the propagation of the first perturbation size and velocity is of interest to advance its numerical modeling. Therefore, the images obtained from the bottom side enhance the knowledge about the phenomenon and the dynamics of the droplet-film impact leading to bubble encapsulation.

In Vasconcelos et al. (2019), the impact conditions where bubble encapsulation was observed were numerically tested to predict the results reported in a previous work (Ribeiro et al., 2018), but despite the inward bending of the crown sheet, it never closed in the simulations. Although the simulations were 2D axisymmetric, the results evidence the need for a better understanding of the dynamic behavior of the first perturbation generated after drop impact. To measure the propagation velocity, the first 12 ms after impact was considered for each dimensionless film thickness between 0.4 and 1. Fig. 9 depicts the evolution of the first perturbation.

Considering $D_p(t)$ as the diameter of the first perturbation, once normalized by the initial drop size ($D_p^* = D_p/D_0$), several authors (Yarin and Weiss, 1995; Cossali et al., 1997; Weiss and Yarin, 1999) scaled the crown radius growth by $D_c^* = D_c/D_0 \sim \tau^{1/2}$. However, the crown angle with the plane of the liquid film (α_c) is lower than $\pi/2$, as required for the morphological steps towards bubble encapsulation. Therefore, since a preliminary analysis of the evolution of the propagation velocity of the first perturbation pointed to $U_p^* = U_p/U_0 \sim \tau^{-1}$, since $dD_p^*/d\tau = U_p^*$, it suggested an evolution for the first perturbation diameter scaled by $D_p^* \sim \ln(\tau)$. Also, without physical boundaries, this first perturbation has no upper limit in its growth, although one physically expects its damping in time while propagating, which is the physical meaning mathematically expressed by the natural logarithm.

Fig. 10 on the left, shows the results for the growth of the first perturbation diameter, normalized by the impact drop diameter. The empirical modeling outcome of this evolution considers a growth depending on the logarithm of dimensionless time and dimensionless film thickness as

$$D_p^*(\delta_f, \tau) = a(\delta_f) + b(\delta_f)\ln(\tau) \tag{1}$$
$$a(\delta_f) = 1.13\delta_f^{-0.197}$$
$$b(\delta_f) = 0.493\ e^{0.612\delta_f}$$
$$\text{valid for } 0.4 \le \delta_f \le 1.0$$

On the right of Fig. 10, the normalized velocity of the first perturbation results in

$$U_p^* = \frac{dD_p^*}{d\tau} = \frac{b(\delta_f)}{\tau} \tag{2}$$

And the results show the validity of this approach.

Fig. 11 shows a comparison between the experimental D_p^* and U_p^* with the values obtained from Eqs. (1) and (2), evidencing the accuracy of the empirical approach explored. These results are useful for future modeling of drop impact conditions leading to bubble encapsulation.

The following, and final section, contains a brief and useful characterization of the bubble geometry, namely, its height and diameter.

3.3. Bubble geometry

The two most evident features of an encapsulated bubble are the bubble height and diameter. To measure the bubble height, the images taken from the side were used and for the bubble diameter the images from below (Fig. 12).

The present experiments allow the investigation of the influence of the dimensionless film thickness on these two features. Since the initial droplet diameter and impact velocity are constant during all the experiments, one can use them as scaling parameters.

The propagation of the first perturbation depended on the dimensionless liquid film. However, the results for the bubble height and

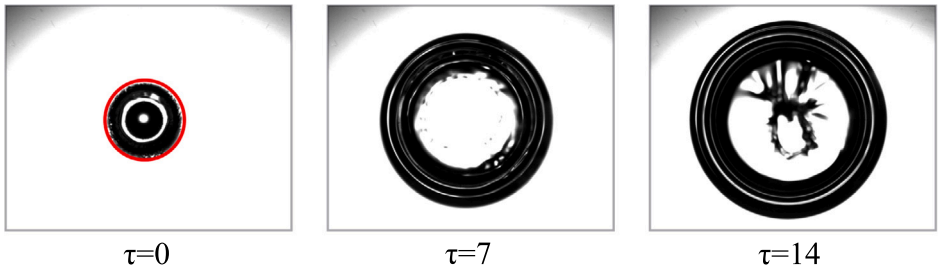

Fig. 9. Sequence of images illustrating the propagation velocity of the first perturbation on the liquid film delimited by the red circle in the first frame. (For interpretation of the references to color in this figure legend, the reader is referred to the web version of this article.)

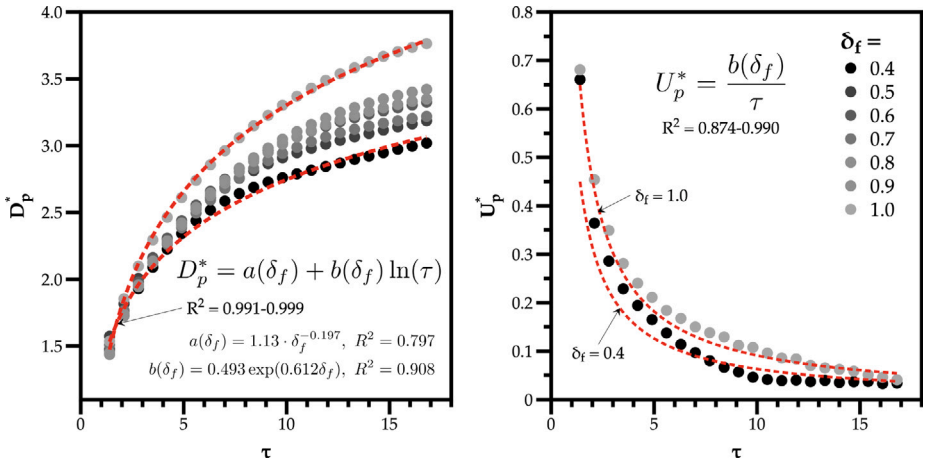

Fig. 10. Evolution of the normalized diameter of first perturbation (D_p^*) and velocity (U_p^*). The curves fitting D_p^*, which depend on the logarithm of time and dimensionless film thickness, are used for modeling U_p^*.

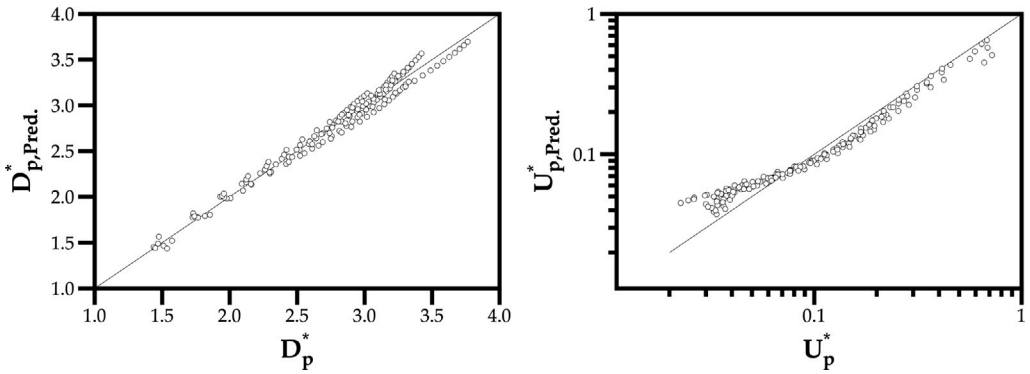

Fig. 11. Comparing the experimental results for D_p^* and U_p^* with the predictions based on the logarithm of time growth of the first perturbation diameter.

diameter synthesized in Fig. 13 show the opposite. The values of bubble height and diameters are detailed in Table 2 in the Appendix, as well as the absolute uncertainty values obtained with a confidence interval of 95%.

When normalized by the initial drop diameter, the normalized bubble height resulted in $h_B^* = h_B/D_0 = 2.4 \pm 0.03$ and the normalized diameter in $D_B^* = D_B/D_0 = 5.8 \pm 0.07$. Both are reasonably independent of the dimensionless film thickness for $0.4 \leq \delta_f \leq 1$. It suggests that the initial impact energy could play a major role in the bubble's characteristic size. Therefore, different impact energies will be tested in future works to assess which dominant features influence bubble size.

4. Conclusions

The present work is dedicated to the encapsulation of a bubble after the single droplet impact onto a thin liquid film resulting from the inward collapse and closure of a splashing crown liquid sheet. The phenomenon has been reported in the literature, but accurate knowledge of the morphological dynamic characteristics is lacking. This study aims to overcome this lack.

Bubble encapsulation (BE) was experimentally investigated for a constant $We_D = 1650$ and a range of $0.1 \leq \delta_f \leq 1$ and captured both from a lateral and a bottom perspective. For the thinner liquid films ($\delta_f = 0.1$), the bubble formation never occurred, and some events

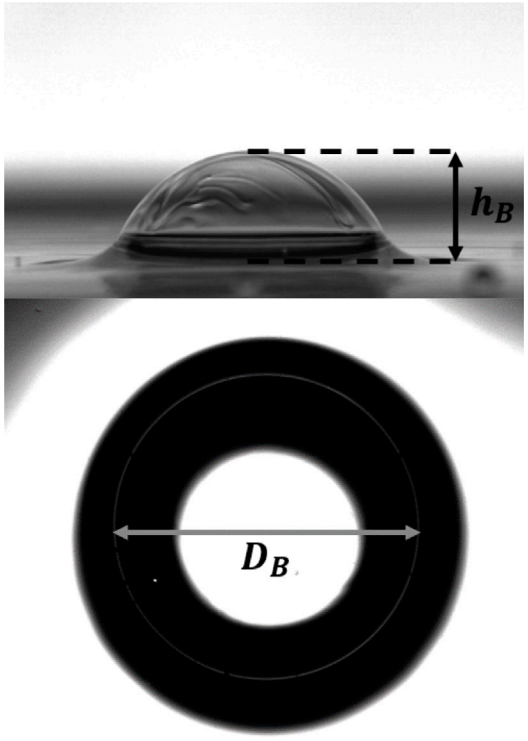

Fig. 12. Measurements of bubble height (h_B) and diameter (D_B).

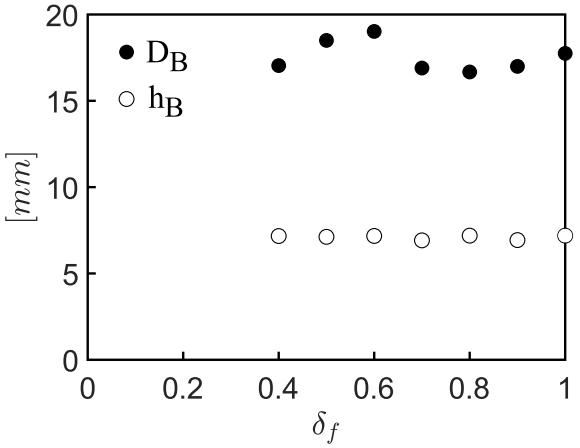

Fig. 13. Bubble height h_B and diameter D_B depending on the dimensionless thickness of the liquid film δ_f.

were seen for $\delta_f = 0.2$ and $\delta_f = 0.3$. The hypothesis is that shallower liquid films do not supply enough momentum to the crown liquid sheet to facilitate its enclosure. For $0.4 \leq \delta_f \leq 1$ resulted in 100% occurrence of BE and the crown sheet angle was normal to the horizontal liquid film in the first stages of splashing. Then, at a fixed height, the crown liquid sheet continues to expand, although the bounding rim does not, which, eventually, is what promotes its enclosure inwards. Three different phenomenologies of bubble encapsulation were observed. Another morphological result shows the effect of increasing the liquid film thickness that thickens the hemispherical bubble dome. The liquid in the hemispherical sheet progressively drains through the dome, thinning the bubble, and enhancing its susceptibility to break. Therefore, the encapsulated bubble's lifetime strongly depends on the number of secondary droplets impinging on its dome, disrupting it when thin enough, and bursting into tertiary atomization, plus intense interference wavy patterns in the area previously delimited by the bubble's dome.

Quantitatively, this work analyzes the morphological dynamic characteristics of the first perturbation generated, propagating after drop impact on the liquid film. A new empirical correlation for the growth of the normalized perturbation's diameter (D_p^*) is proposed based on the logarithm of the normalized time (τ) and coefficients that depend on the dimensionless film thickness (δ_f), $D_p^* = a(\delta_f) + b(\delta_f)\ln(\tau)$. However, when quantifying the final bubble height (h_B) and diameter (D_B), relative to the initial drop diameter (D_0), the results are independent of the dimensionless film thickness. Future research includes the development of a criterion for the onset of bubble encapsulation based on the characteristics of the impinging droplet and the liquid film with varying thermophysical properties.

CRediT authorship contribution statement

Daniela F.S. Ribeiro: Conceptualization, Methodology, Software, Validation, Formal analysis, Investigation, Data curation, Writing – original draft, Visualization. **Miguel R.O. Panão:** Conceptualization, Formal analysis, Resources, Writing – review & editing, Supervision. **Jorge M.M. Barata:** Resources, Supervision, Project administration, Funding acquisition. **André R.R. Silva:** Conceptualization, Resources, Writing – review & editing, Supervision, Project administration, Funding acquisition.

Declaration of competing interest

The authors declare that they have no known competing financial interests or personal relationships that could have appeared to influence the work reported in this paper.

Data availability

Data will be made available on request

Acknowledgments

The present work was performed under the scope of Aeronautics and Astronautics Research Center (AEROG) of the Laboratório Associado em Energia, Transportes e Aeronáutica (LAETA) – activities and it was supported by Fundação para a Ciência e a Tecnologia (FCT), Portugal through the project UID/EMS/50022/2020 and also by the Ph.D. scholarship, Portugal with the reference SFRH/BD/140009/2018. Miguel Oliveira Panão would like to acknowledge projects UIDB/50022/2020 and UIDP/ 50022/2020 of ADAI for the support provided for this publication.

Appendix

See Table 2.

Table 2
Data of bubble height and diameter for different dimensionless film thicknesses. The uncertainty values are absolute and obtained with a confidence interval of 95%.

δ_f	h_B [mm]	D_B [mm]
0.4	7.2 ± 0.009	17.0 ± 0.008
0.5	7.1 ± 0.024	18.5 ± 0.016
0.6	7.2 ± 0.010	19.0 ± 0.018
0.7	6.9 ± 0.005	16.9 ± 0.021
0.8	7.2 ± 0.007	16.7 ± 0.010
0.9	6.9 ± 0.006	17.0 ± 0.016
1.0	7.2 ± 0.002	17.7 ± 0.018

References

Cossali, G.E., Coghe, A., Marengo, M., 1997. The impact of a single drop on a wetted solid surface. Exp. Fluids 22 (6), 463–472.

Engel, O.G., 1966. Crater depth in fluid impacts. J. Appl. Phys. 37 (4), 1798–1808.

Fedorchenko, A.I., Wang, A.-B., 2004. On some common features of drop impact on liquid surfaces. Phys. Fluids 16 (5), 1349–1365.

Ferrão, I., Vasconcelos, D., Ribeiro, D., Silva, A., Barata, J., 2020. A study of droplet deformation: The effect of crossflow velocity on jet fuel and biofuel droplets impinging onto a dry smooth surface. Fuel 279, 118321. http://dx.doi.org/10.1016/j.fuel.2020.118321, URL: https://www.sciencedirect.com/science/article/pii/S001623612031317X.

Geppert, A., Chatzianagnostou, D., Meister, C., Gomaa, H., Lamanna, G., Weigand, B., 2016. Classification of impact morphology and splashing/deposition limit for N-Hexadecane. At. Sprays 26 (10), 983–1007.

Guo, J.-H., Dai, S.-Q., Qin, D., 2010. Experimental research on the droplet impacting on the liquid film. Acta Phys. Sin. 59 (4), 2601–2609.

Lamanna, G., Geppert, A., Bernard, R., Weigand, B., 2022. Drop impact onto wetted walls: an unsteady analytical solution for modelling crown spreading. J. Fluid Mech. 938, A34. http://dx.doi.org/10.1017/jfm.2022.69.

Liang, G., Mudawar, I., 2016. Review of mass and momentum interactions during drop impact on a liquid film. Int. J. Heat Mass Transfer 101, 577–599.

Motzkus, C., Gensdarmes, F., Géhin, E., 2009. Parameter study of microdroplet formation by impact of millimetre-size droplets onto a liquid film. J. Aerosol Sci. 40 (8), 680–692.

Ninomiya, N., Iwamoto, K., 2012. PIV measurement of a droplet impact on a thin fluid layer. In: AIP Conference Proceedings, Vol. 1428. pp. 11–17.

Pan, K.-L., Cheng, K.-R., Chou, P.-C., Wang, C.-H., 2008. Collision dynamics of high-speed droplets upon layers of variable thickness. Exp. Fluids 45 (3), 435–446.

Pan, K.-L., Hung, C.-Y., 2010. Droplet impact upon a wet surface with varied fluid and surface properties. J. Colloid Interface Sci. 352 (1), 186–193.

Ribeiro, D., Cunha, N., Barata, J., Silva, A., 2018. Dynamic behaviour of single droplets impinging upon liquid films with variable thickness: Jet A-1 and HVO mixtures. In: 14th International Conference on Liquid Atomization & Spray Systems, July 22-26. p. 8pp..

Ribeiro, D., Panao, M.O., Barata, J.M., Silva, A.R., 2020a. Morphology of bubble formation on droplet impact upon thin liquid layers. In: AIAA Scitech 2020 Forum. p. 1577.

Ribeiro, D.F.S., Silva, A.R.R., Panão, M.R.O., 2020b. Insights into single droplet impact models upon liquid films using alternative fuels for aero-engines. Appl. Sci. 10 (19), http://dx.doi.org/10.3390/app10196698, URL: https://www.mdpi.com/2076-3417/10/19/6698.

Roisman, I.V., van Hinsberg, N.P., Tropea, C., 2008. Propagation of a kinematic instability in a liquid layer: capillary and gravity effects. Phys. Rev. E 77 (4), 046305.

Vasconcelos, D., Ribeiro, D., Barata, J.M., Silva, A.R., 2019. Experimental and numerical study of single droplets impinging upon liquid films. In: 4th Thermal and Fluid Engineering Conference, April 14-17. p. 4pp.

Wang, A.-B., Chen, C.-C., 2000. Splashing impact of a single drop onto very thin liquid films. Phys. Fluids 12 (9), 2155–2158.

Weiss, D.A., Yarin, A.L., 1999. Single drop impact onto liquid films: neck distortion, jetting, tiny bubble entrainment, and crown formation. J. Fluid Mech. 385, 229–254.

Worthington, A.M., 1908. A Study of Splashes. Longmans, Green, and Company.

Yarin, A.L., Weiss, D.A., 1995. Impact of drops on solid surfaces: self-similar capillary waves, and splashing as a new type of kinematic discontinuity. J. Fluid Mech. 283, 141–173.